

Development of AlN_x films for superconducting quantum circuits

Author: Ariadna Gómez del Pulgar Martínez

Facultat de Física, Universitat de Barcelona, Diagonal 645, 08028 Barcelona, Spain.

Advisors: Alba Torras Coloma, Pol Forn-Díaz and Francesca Peiró Martínez

Abstract: A promising material to achieve high inductance and low dissipation in superconducting quantum circuits is aluminum nitride, which has not been previously studied as a superinductor. In this project, aluminum nitride thin films have been fabricated and characterized and microwave resonators have been simulated as the first step of an experiment that will demonstrate aluminum nitride's superinductor properties.

I. INTRODUCTION

Superconducting qubits are presently the lead system to build a quantum computer [1]. In order to reach large-scale devices, a high-impedance medium presents interesting opportunities to enhance coherence time and quantum gate fidelity. An easily implementable method for doing so are superinductors, which are materials that naturally showcase a high kinetic inductance [2].

Materials that commonly present a high kinetic inductance are disordered superconductors and, especially, granular superconductors. An example of these materials is granular aluminum (grAl). Granular aluminum consists of an aluminum oxide matrix filled with aluminum grains that connect to each other via Josephson tunneling [3]. GrAl has been proven to be a superinductor and to improve quantum circuit operation while demonstrating a high internal quality factor [2, 4]. Due to the extended use of nitrides in superconducting circuits (NbN, TiN...), a promising candidate to be a superinductor is aluminum nitride (AlN_x). AlN_x is expected to cause a higher noise reduction in quantum circuits than grAl. The superconducting properties of this material, however, are still to be proven.

In this work, I will characterize AlN_x thin films with different nitrogen content and simulate several resonators that, in the future, can be fabricated and tested to demonstrate the attributes of AlN_x and other materials as superinductors. Sec. II presents the theoretical basis to estimate the kinetic inductance of AlN_x and the resonant frequency of the resonators considered. Sec. III gives experimental details about thin film growth and the simulation workflow. Finally, experimental and simulation results are summarized and discussed in Sec. IV.

II. THEORETICAL BACKGROUND

A. Kinetic inductance and sheet resistance

Kinetic inductance, L_k , is the inductance contribution that emerges from the kinetic energy associated with the movement of current carriers when establishing a current in the interior of a conducting strip. In superconducting metals, it can sometimes be the main source of induc-

tance [5, 6]. As a first guess, we can approximate the kinetic inductance per square of AlN_x as [4]

$$L_{kin,\square} = \frac{0.18\hbar R_n}{k_B T_c}, \quad (1)$$

where R_n is the normal state sheet resistance of the studied film and T_c is the critical temperature of the superconductor [7]. In our particular case, we do not know its value for AlN_x , but as an approximation we will use pure aluminum's critical temperature, as we expect a value of the similar order for AlN_x , as it happens with grAl: $T_{c,Al} = 1.19$ K. On the other hand, the normal state sheet resistance is defined as the sheet resistance of a certain film at a temperature of 4 K. Once again, we do not know its value beforehand, so it has been estimated as the sheet resistance at room temperature, which seems to be a good approximation for disordered superconductors. Sheet resistance is defined as [8]

$$R_s = \frac{\rho}{t}, \quad (2)$$

where ρ is the resistivity of the given film [9] and t is its thickness. Resistivity is a measure of the opposition that a material presents to the flow of charge, and it can be used to discern metals from insulators. In our case, ρ will be used to determine at which concentration of nitrogen the mixture shifts from a metal to an insulator and to detect similarities between this material and granular aluminum. Moreover, it is around the metal-to-insulator transition region where we expect the superconductor to become a superinductor.

B. Resonators

In this work, three different types of resonators will be used: lumped-element RLC parallel circuits, coplanar $\lambda/4$ waveguides and microstrip $\lambda/2$ resonators. Some examples of them are shown in Fig.(1).

A lumped-element parallel resonator consists on a parallel RLC circuit in which the dimensions of every part of the circuit are much smaller than the wavelength of the electromagnetic waves. In our case, the inductor, L , is a meandered inductor, the capacitor, C , is an interdigitated capacitor, and the resistor, R , is an equivalent

resistance that accounts for conductor, dielectric and radiation losses that occur in the inductance and the capacitor [6, 10]. The inductor, placed at the bottom, and capacitor, placed on top, can be seen in Fig.(1)(a, b). Resonance happens at the frequency for which the input impedance of the circuit is purely real, or, equivalently, when the time-averaged stored electric and magnetic energies are equal. For an RLC lumped-element circuit, the resonant frequency is [6, 10]

$$\omega_0 = \frac{1}{\sqrt{LC}}. \quad (3)$$

$\lambda/4$ and $\lambda/2$ resonators are sections of thin-film transmission line of length l that satisfy that, at resonance, $l = \lambda_0/4$ and $l = \lambda_0/2$, respectively, where λ_0 is the wavelength corresponding to the resonant frequency. The waves traveling through these devices can be considered as transverse electromagnetic (TEM) waveguides [10]. These resonators are distributed-element circuits, which means that their dimensions are a considerable fraction of the employed wavelength or even several wavelengths [10]. The $\lambda/4$ resonators were implemented as coplanar waveguides (CPW), surrounded by ground, open-circuited at one end and short-circuited at the other end, whereas the $\lambda/2$ are microstrips open-circuited at both ends [11]. The first resonant mode occurs for

$$f_{0,\lambda/4} = \frac{c}{4l\sqrt{\varepsilon_{eff}}}, \quad f_{0,\lambda/2} = \frac{c}{2l\sqrt{\varepsilon_{eff}}}, \quad (4)$$

where c is the speed of light in vacuum and ε_{eff} is the effective relative permittivity of the transmission lines. For frequencies close to resonance, both resonators show a similar behavior to that of lumped-element parallel RLC circuits, and therefore their first resonant frequency can be calculated as Eq.(3), with effective L and C [6, 10].

In our particular devices, the power is driven into the lumped-element and $\lambda/4$ resonators via a CPW feedline, which has a characteristic impedance $Z_0 = 50 \Omega$. The coupling between the resonators and the line is inductive [6, 12]. For the $\lambda/2$ resonators, however, the power is driven by introducing them in a rectangular copper cavity, with two SMA ports, that will present resonant modes as well [10].

A useful method to experimentally find the resonant frequency of a microwave circuit are the so-called S parameters, which illustrate transmission and reflection of two-port networks [6, 10]. For the lumped-element parallel circuits and $\lambda/4$ resonators, the magnitude of S_{21} of the feedline presents a minimum at resonance, whereas for $\lambda/2$ resonators there is a minimum in the magnitude of S_{11} at resonance (see Appendix). Apart from the resonant frequency, we can extract the quality factor, Q , from the S parameters, as the latter have a Lorentzian dependency on frequency. This parameter reflects the losses in the measured device and can be computed as the resonant frequency divided by the full-width half-maximum [10].

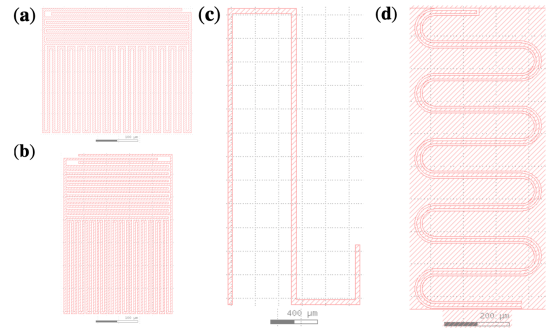


FIG. 1: Different resonators used in this work. (a) First design of lumped-element resonators. (b) Second design of lumped-element resonators. (c) $\lambda/2$ resonators. (d) $\lambda/4$ resonators.

III. METHODOLOGY AND SIMULATIONS

Different AlN_x wafers were first fabricated by sputtering [13] at IMB-CNM-CSIC with different concentrations of Ar and N and measured in order to determine their sheet resistance and other basic properties. As for their measurements, their sheet resistance was determined via the Van der Pauw method [8] and their thickness was measured with a profilometer and different SEM images. The data obtained from the measurements of AlN_x films in Table I was used to perform the simulations of the resonators.

There are 44 resonators in total to be simulated: 20 lumped-element resonators, divided into two different designs, 10 $\lambda/4$ resonators, and 14 $\lambda/2$ resonators. The length of the last two or three fingers, depending on the design, of the capacitor of the lumped-element resonators varies at each device, and the total length of the distributed-element resonators changes from one device to another. A selection of them is shown in Fig.(1). [18].

The simulations determine a first approximation of the resonances to be expected and whether or not the IFAE laboratory equipment, which can measure between 1 and 8 GHz, is able to reach those values.

Two software platforms were used so as to determine the resonant frequencies of all our devices: COMSOL Multiphysics [14] and Sonnet [15]. COMSOL was used to determine the resonant frequency of the cavity, which is necessary to discern it from that of the resonators, via the RF Module and the guidelines included in [16], adapted to our specific device. A thorough description of the model is included in Appendix.

To contrast the results of these simulations with the actual physical cavity, the latter was measured in the laboratory by means of a Vector Network Analyzer (VNA) [10], shown in Fig.(3). From the obtained data, we were able to determine its first resonant frequency and its loaded quality factor via a code that was written (see Appendix).

On the other hand, Sonnet was used to simulate the RLC , $\lambda/4$ and $\lambda/2$ resonators. The implemented models

and simulation process are presented in Appendix.

IV. RESULTS

A. Kinetic inductance of AlN_x

The sheet resistance and thickness of AlN_x films were determined as explained in Sec. III, while their resistivity was obtained from Eq.(2) and their kinetic inductance per square was approximated as Eq.(1).

Some results presented in Table I are shown in a range for a given concentration of nitrogen. This is due to the fact that R_s and ρ were not uniform across the entirety of the surface: their values seemed to be lower at the edges of the wafer. A possible cause is that the thickness may not be as consistent as previously thought. Moreover, the width of the range increases with higher amounts of nitrogen. That indicates that this inhomogeneity increases with increasing concentration of nitrogen, perhaps due to increasing granularity.

From Fig. (2), we can clearly differentiate three distinct regions according to AlN_x resistivity as a function of the concentration of nitrogen. The first one covers percentages between 0 and 7.5-10% of N and shows a lower value of resistivity, which indicates that the material behaves as a metal. There is a second region that ranges from 10% to 15-20%, at which AlN_x has a much larger value of resistivity. This region can be understood as the transition region from metal to insulator. Finally, above 15-20% the resistivity is not measurable, which means that the material is showing an insulator behavior and can be considered to be fully nitrized.

From the data presented in Table I, AlN_x might be, in fact, a superinductor, reaching values of kinetic inductance of several nH per square, which was the main hypothesis and motivation for this work.

With the aim of carrying out a more detailed depiction of the different ρ values of AlN_x and, especially, to study the transition region, the concentrations 5%, 7.5%, 10%

| % of N | R_s ($\frac{\Omega}{\square}$) | t (nm) | ρ ($\mu\Omega \cdot \text{cm}$) | $L_{kin,\square}$ ($\frac{\text{pH}}{\square}$) |
|--------|------------------------------------|----------|--|---|
| 0 | 0.15 | 228 | 3.42 | 0.17 |
| 3.75 | 2.45 | 96.2 | 23.569 | 2.8 |
| 5 | 3.55 | 100 | 35.5 | 4.1 |
| 7.5 | 2.58 | 101.6 | 26.2128 | 3 |
| 10 | 14.5 | 83 | 120.4 | 16.5 |
| 11.7 | 24-32 | 97 | 233-310 | 27.7 - 37 |
| 13.3 | 84-120 | 94.6 | 795-1135 | 97 - 138.6 |
| 14.2 | 216-498 | 97.3 | 2101-4845 | 249.6 - 575.4 |
| 15 | 950-3170 | 127 | 12065-40259 | 1097.6 - 3662.5 |
| 20 | Not meas. | 47 | - | - |

TABLE I: Values for sheet resistance, thickness, resistivity and kinetic inductance per square for different concentrations of nitrogen during the sputtering process.

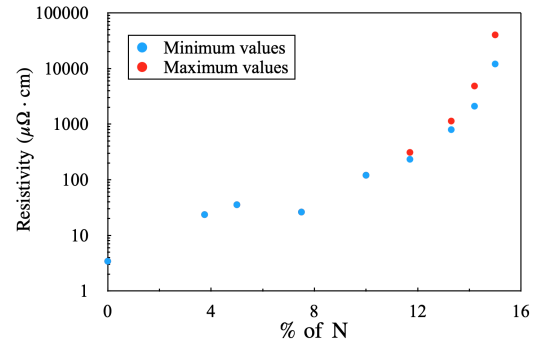


FIG. 2: Resistivity of AlN_x as a function of the concentration of nitrogen, according to the data presented in Table I.

and 11.7% where chosen as those to be used in the forthcoming simulations. For this last percentage, the average between the minimum and maximum values of obtained kinetic inductance was used as a first approximation.

B. Cavity simulations

The resonant frequency of the physical cavity was found to be $f_0 = 7.5327$ GHz, and its quality factor was determined as $Q = 5332$. On the other hand, the resonant frequency extracted from the simulations was $f_0 = 7.5715$ GHz, and its quality factor was $Q = 5824$. Although the plots presented in Fig.(3) are slightly different in terms of the reached $|S_{21}|$ values, the resonant frequency and quality factor obtained from the simulations are similar to those of the physical cavity. The difference between them, however, might be a consequence of the dimensions of the simulated cavity not accurately matching those of the actual cavity, an effect of the external circuitry introduced by the presence of the VNA or any other conductor losses that have not been properly introduced in the model.

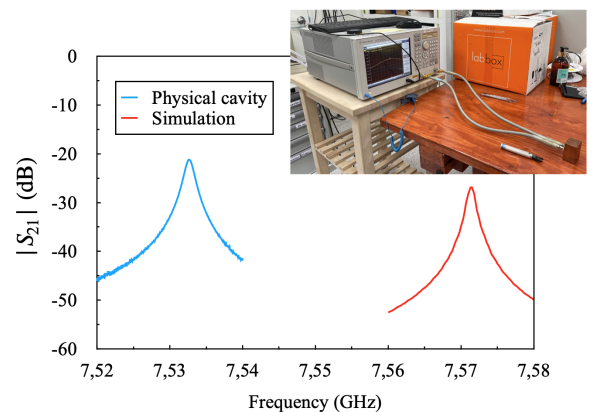


FIG. 3: $|S_{21}|$ as a function of frequency of the copper cavity, according to the data obtained from the VNA measurements and the COMSOL simulations. As an inset, setup of the VNA measurements.

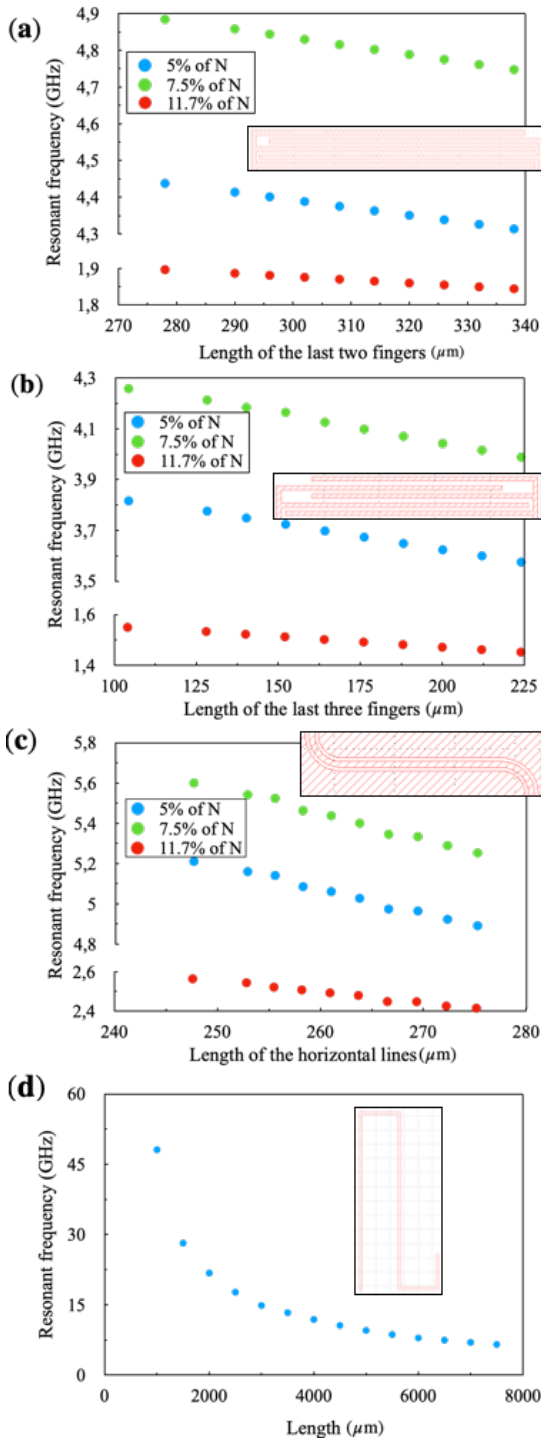


FIG. 4: Resonant frequency as a function of the geometric features that vary from one resonator to another, depicted as insets, according to the data obtained from the Sonnet simulations, for different concentrations of nitrogen. (a) First lumped-element resonators. (b) Second lumped-element resonators. (c) $\lambda/4$ resonators. (d) $\lambda/2$ resonators, for a concentration of 10% of N.

C. Resonator simulations

From Fig.(4)(d), we can clearly see that the resonant frequency of the $\lambda/2$ resonators follows the hyperbolic dependence pointed in Eq.(3), as expected. However, the resonant frequencies of the lumped-element and $\lambda/4$ resonators follow a linear distribution. The reason for this unexpected behavior relies on the design and definition of the resonators. For the lumped-element ones, the linear dependence might just be a fortuity, and it can, indeed, be much more complicated than it seems and only locally linear. In this case, what changes at every device is the length of two or three fingers, thus modifying the capacitance of the resonator. However, this variations might follow a not even analytically solvable expression, contrary to what happens when all the fingers shift [17]. On the other hand, for the $\lambda/4$ resonators, as their resonant frequency satisfies that of Eq.(4), the different lengths of the resonators were chosen with the purpose of having a linear dependence. Nonetheless, we stress from Fig.(4)(a-c) that the frequencies are higher when the kinetic inductance is lower, and conversely, which reflects the dependency of the resonant frequency shown in Eq.(3).

Additionally, from the distribution of currents at resonance shown in Fig.(5) we can confirm the expected behavior of each resonator: the $\lambda/2$ ones show half a wavelength, with two minima at the ends of the resonator and a maximum between them, the $\lambda/4$ ones show a quarter of a wavelength, with a minimum at one end and a maximum at the other end, and the lumped-element ones have their charge in the inductor [6].

Another confirmed distinctive trait of each resonator is depicted in Fig.(6), showing the minima of $|S_{11}|$ and $|S_{21}|$ that were expected at resonance for the $\lambda/2$ resonators and the $\lambda/4$ and lumped-element resonators, respectively.

From the range of obtained frequencies, we can conclude that, at least at a first glance, all lumped-element and $\lambda/4$ resonators and the 4 longer $\lambda/2$ resonators can be measured with the available machinery at the facilities of IFAE.

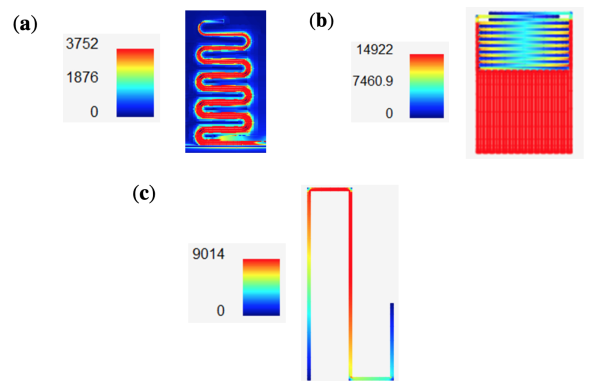


FIG. 5: Distribution of currents at resonance of the resonators in Fig.(1). The scale is in amps/meter. (a) $\lambda/4$ resonators. (b) First lumped-element resonators. (c) $\lambda/2$ resonators.

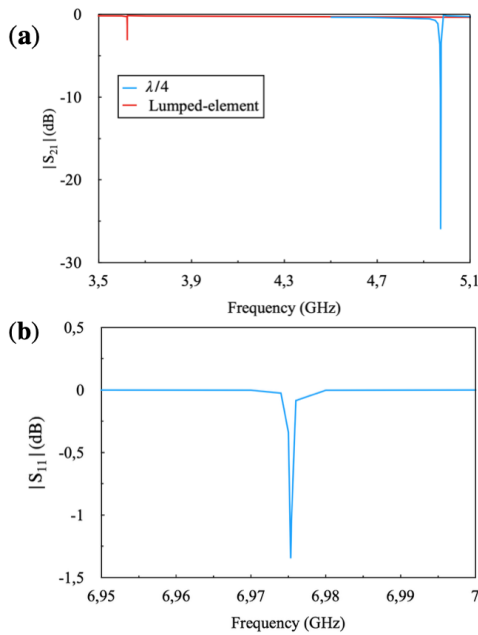


FIG. 6: Minima of the corresponding S parameters of the resonators in Fig.(5). (a) First lumped-element and $\lambda/4$ resonators. (b) $\lambda/2$ resonators.

V. CONCLUSIONS

The most relevant outcome of this work is the apparent superinducting behavior of aluminum nitride. Whether or not AlN_x is, indeed, a superinductor, still remains to be clarified by the experimental realization of the simulated resonators. These simulations have shown that all

the lumped-element and $\lambda/4$ resonators and 4 of the $\lambda/2$ resonators are measurable with the laboratory equipment at IFAE, up to 8 GHz.

Furthermore, COMSOL and Sonnet have been proven to be exceptional simulation software tools, as the simulation of the cavity has shown. Their performance, however, could be improved. In the case of Sonnet, that could be done by using a smaller meshing for the lumped-element resonators and conformal meshing for the $\lambda/4$ resonators and further narrowing the simulation sweeps. For COMSOL, it is advisable to simulate both the cavity and the resonators as a single system to see if their resonant frequencies are affected by being coupled.

The next steps to follow are to fabricate the resonators that have been pointed as measurable from the simulations and to measure them at low temperature at the dilution refrigerators of the laboratory. From their resonant frequency, the kinetic inductance of AlN_x will be ascertained. Other parameters that will be extracted as well are the normal state sheet resistance of the films and the critical temperature of AlN_x .

The ultimate stage of this work is to incorporate AlN_x in superconducting quantum circuits, which will, at last, demonstrate the enhancement that aluminum nitride is expected to occasion to quantum gate algorithms.

Acknowledgments

I would like to thank my tutors for their invaluable advise and indefatigable help, as well as the QCT, Qilimanjaro and CNM teams for aiding when needed.

-
- [1] Krantz, P. et al., *A Quantum Engineer's Guide to Superconducting Qubits*. Applied Physics Reviews **6**: 021318 (2019).
 - [2] Grünhaupt, L., *Granular Aluminum Superinductors* (KIT Scientific Publishing, Karlsruhe, 2019).
 - [3] Tafuri, F., *Fundamentals and Frontiers of the Josephson Effect*, Springer Series in Materials Science **286** (2019).
 - [4] Valenti, F. et al., *Interplay Between Kinetic Inductance, Nonlinearity, and Quasiparticle Dynamics in Granular Aluminum Microwave Kinetic Inductance Detectors*. Phys. Rev. Applied **11**: 054087 (2019).
 - [5] Van der Sar, T., *Kinetic Inductance of Aluminum Wires* (University of Delft, 2005).
 - [6] Doyle, S., *Lumped Element Kinetic Inductance Detectors* (University of Cardiff, 2005).
 - [7] Kresin, V. Z. and Wolf, S. A., *Fundamentals of Superconductivity*, 1st ed. (Springer, Boston, MA, 1990).
 - [8] Miccoli, I. et al., *The 100th anniversary of the four-point probe technique: the role of probe geometries in isotropic and anisotropic systems*. J. Phys.: Condens. Matter **27**: 223201 (2015).
 - [9] Streetman, B. G. et al., *Solid State Electronic Devices*, 7th ed. (Pearson, New York, NY, 2014).
 - [10] Pozar, D. M., *Microwave Engineering*, 4th. ed. (John Wiley & Sons, Amherst, MA, 1975).
 - [11] Zmuidzinas, J., *Superconducting Microresonators: Physics and Applications*. Annu. Rev. Condens. Matter Phys. **3**: 169-214 (2012).
 - [12] Houdart, M., *Coplanar Lines: Application to Broadband Microwave Integrated Circuits*. 6th European Microwave Conference (1976).
 - [13] Vossen, J. L. et al., *Thin Film Processes II*, 1st ed. (Academic Press, Cambridge, MA, 1991).
 - [14] <https://www.comsol.com>.
 - [15] <https://www.sonnetsoftware.com>.
 - [16] <https://www.comsol.com/model/coaxial-to-waveguide-coupling-1863>.
 - [17] Guo, J. et al, *Optimization and experimental verification of coplanar interdigital adhesives*. J. Phys. D: Appl. Phys. **49**: 415304 (2016).
 - [18] The resonators were designed by David López Núñez and Boris Nedyalkov, current PhD students of the QCT group at IFAE.

VI. APPENDIX

A. Scattering parameters

The *scattering parameters* or *S parameters* are defined for a two-port network as [10]

$$S_{11} = \frac{V_1^-}{V_1^+} \quad S_{21} = \frac{V_2^-}{V_1^+}$$

$$S_{12} = \frac{V_1^-}{V_2^+} \quad S_{22} = \frac{V_2^-}{V_2^+},$$

where V_n^+ represents the voltage wave incident at the port n and V_n^- symbolises the voltage wave excited from the port n . We stress that, generally, these parameters are complex numbers and will have a certain amplitude and phase.

An easier approach to the scattering parameters can be achieved by the *transmission matrix* or *ABCD matrix*, another describing factor of two-port networks. This matrix satisfies that [10]

$$\begin{bmatrix} V_1 \\ I_1 \end{bmatrix} = \begin{bmatrix} A & B \\ C & D \end{bmatrix} \begin{bmatrix} V_2 \\ I_2 \end{bmatrix},$$

where V_1 and I_1 represent the voltage and current at port 1, whereas V_2 and I_2 represent the voltage and current at port 2.

The conversion between the ABCD matrix of a microwave two-port network and its corresponding S parameters is [10]

$$S_{11} = \frac{A + B/Z_0 - CZ_0 - D}{A + B/Z_0 + CZ_0 + D},$$

$$S_{12} = \frac{2(AD - BC)}{A + B/Z_0 + CZ_0 + D},$$

$$S_{21} = \frac{2}{A + B/Z_0 + CZ_0 + D},$$

$$S_{22} = \frac{-A + B/Z_0 - CZ_0 + D}{A + B/Z_0 + CZ_0 + D}.$$

The input impedance of open-circuited $\lambda/2$ resonators for frequencies close to that of resonance (that is, frequencies of the form $\omega = \omega_0 + \Delta\omega$, where $\Delta\omega$ is small) is [10]

$$Z_{in} \approx \frac{Z_0}{\alpha l + j \left(\frac{\Delta\omega\pi}{\omega_0} \right)}.$$

From this equation, the analogy between $\lambda/2$ resonators and lumped-element *RLC* parallel circuits is clear, as, for the latter [10],

$$Z_{in} \approx \frac{1}{\frac{1}{R} + 2j\Delta\omega C}.$$

Each type of circuit has a different ABCD matrix. $\lambda/2$ open-circuited resonators can be considered as shunt admittances, due to their similarities with lumped-element *RLC* parallel circuits. For these circuit elements, the ABCD matrix takes the form of [10]

$$\begin{bmatrix} 1 & 0 \\ Y & 1 \end{bmatrix},$$

where Y is the admittance of the circuit, which is $Y = \frac{1}{Z_{in}}$.

For the $\lambda/2$ resonators, we obtain the parameters

$$S_{11} = S_{22} = -\frac{YZ_0}{2 + YZ_0} = -\frac{\alpha l + j \frac{\Delta\omega\pi}{\omega_0}}{2 + \alpha l + j \frac{\Delta\omega\pi}{\omega_0}} \implies$$

$$|S_{11}|^2 = |S_{22}|^2 = \frac{(\alpha l)^2 + \left(\frac{\Delta\omega\pi}{\omega_0} \right)^2}{(2 + \alpha l)^2 + \left(\frac{\Delta\omega\pi}{\omega_0} \right)^2},$$

$$S_{12} = S_{21} = \frac{2}{2 + YZ_0} = \frac{2}{2 + \alpha l + j \frac{\Delta\omega\pi}{\omega_0}} \implies$$

$$|S_{12}|^2 = |S_{21}|^2 = \frac{4}{(2 + \alpha l)^2 + \left(\frac{\Delta\omega\pi}{\omega_0} \right)^2}.$$

From these last equations, for $\Delta\omega = 0$, which corresponds to resonance, $|S_{11}|^2$ presents a minimum and $|S_{12}|^2$ presents a maximum.

For the lumped-element and $\lambda/4$ resonators, the reasoning is different, as the power is driven to them via a feedline and it is the transmission and reflection of the latter, and not the resonators, that is studied. The resonators present a certain input impedance, which has a maximum value at resonance [10]. Due to this input impedance, the resonators take power from the feedline, presenting a higher leakage at resonance [10]. Because of that, the transmission of the feedline, represented by its S_{21} and S_{12} parameters, will have a minimum when resonance occurs, as the input impedance is maximum. A thorough explanation of this phenomenon, by considering the effective impedance of the entire resonant section and finding its S parameters and ABCD matrix, is included in [6]. We note that, for the $\lambda/2$ resonators, their input impedance is maximum at resonance as well, and this can also explain the minimum in their transmission parameters.

resonator and the ground is odd, for the second lumped-element and $\lambda/4$ resonators it was of $2 \mu\text{m}$, as the smallest distances was $4 \mu\text{m}$, and for the $\lambda/2$ resonators it was $20 \mu\text{m}$. The use of conformal meshing for the $\lambda/4$ resonators, as it is recommended in the Sonnet documentation for curved elements, was discarded as it drastically increased the simulation time from 30 minutes to 8 hours while only introducing changes in the second decimal of the resonant frequency.

After defining the cell size, it is relevant to make sure that all the vertices and lines of our geometry coincide with vertices of the meshing. If this does not happen, the simulation time will be negatively affected.

At this point, the only remnant thing to do to complete the geometry of the resonator is to add the two ports of the network, which have to be placed at the sides of the box. For the resonators that lie next to the feedline, the ports were placed at the edges of the feedline, whereas for the $\lambda/2$ ones we placed them just above and below the resonator.

The next step is to define the different materials that conform our sample. For the substrate, “Silicon (intrinsic)” was selected from the library available at Sonnet and set the dielectric loss \tan to be $5.5 \cdot 10^{-5}$ and the conductivity to be of 0 S/m . The thickness of the material was of $500 \mu\text{m}$, which is the usual thickness of the substrate of any chip. The rest of the parameters should remain untouched. On the other hand, for the metal layer “Aluminum” was chosen from the available library

as the planar metal to use. The “General” model was selected, which is appropriate for models of infinitesimal height that can be modeled as a 2D sheet. All the parameters that account for resistance were set to be 0, as the experimental measurements will be done in the range of temperatures for which AlN_x behaves as a superconductor and therefore its resistance is null. However, the sheet inductance was modified according to Table I, depending on the different percentages of N desired to portray. Lastly, the top material of the sample was defined as “Air”. Any parameters have to be changed, apart from setting the thickness to be of $5000 \mu\text{m}$.

The last step before starting the simulation is to define the frequency sweeps. They were performed as adaptive sweeps and the currents were computed too. After the first simulation is performed, it needs to be refined. This is achieved by changing the frequency in the sweep, shortening the range around the resonant frequency. Once we have narrowed the range enough, we can make use of the current computation to find the exact resonant frequency as the one that makes the currents to be stronger and reach a higher value. The sweeps of the lumped-element resonators have to be around smaller values so as not to excite non-desired distributed-element resonant modes.

These simulations were performed at the Port d’Informació Científica server in order to minimize the simulation time.